# A combined EXAFS, XRD, DRIFTS and DFT study

# of nano copper-based catalysts for CO₂ hydrogenation

*Marco Bersani[‡,1], Kalyani Gupta[‡,1], Abhishek Kumar Mishra[1], Roberto Lanza[2], S.F. Rebecca Taylor[3], Husn-Ubayda Islam[4], Nathan H. Hollingsworth[1], Christopher Hardacre[3], Nora H. de Leeuw[1,4], Jawwad A. Darr*[,1]*

[1]Department of Chemistry, Christopher Ingold Laboratories, University College London, 20 Gordon Street, London, WC1H 0AJ, United Kingdom

[2]Department of Chemical Engineering and Technology, KTH − Royal Institute of Technology, Teknikringen 42, 100 44 Stockholm, Sweden

[3]School of Chemical Engineering and Analytical Science, The University of Manchester, Oxford Road, Manchester, M13 9PL, UK

[4]School of Chemistry, Cardiff University, Main Building, Park Place, Cardiff CF10 3AT, UK

ABSTRACT: Highly monodispersed CuO nanoparticles (NPs) were synthesised via Continuous Hydrothermal Flow Synthesis (CHFS) and then tested as catalysts for $CO_2$ hydrogenation. The catalytic behaviour of unsupported 11 nm-sized nanoparticles from the same batch was characterised by Diffuse Reflectance Infrared Fourier Transform Spectroscopy (DRIFTS), Extended X-Ray Absorption Fine Structure (EXAFS), X-Ray Diffraction (XRD) and catalytic testing, under $CO_2/H_2$ in the temperature range 25 to 500 °C in consistent experimental conditions. This was done to highlight the relationship between structural evolution, surface products and reaction yields; the experimental results were compared with modelling predictions based on Density Functional Theory (DFT) simulations of the CuO system. In-situ DRIFTS revealed the formation of surface formate species at temperatures as low as 70 °C. DFT calculations of $CO_2$ hydrogenation on the CuO surface suggested that hydrogenation reduced the CuO surface to $Cu_2O$, which facilitated the formation of formate. In-situ EXAFS supported a strong correlation between the $Cu_2O$ phase fraction and the formate peak intensity, with the maxima corresponding to where $Cu_2O$ was the only detectable phase at 170 °C, before the onset of reduction to Cu at 190 °C. The concurrent phase and crystallite size evolution were monitored by in-situ XRD, which suggested that the CuO NPs were stable in size before the onset of reduction, with smaller $Cu_2O$ crystallites being observed from 130 °C. Further reduction to Cu from 190 °C was followed by a rapid decrease of surface formate and the detection of adsorbed CO from 250 °C; these results are in agreement with heterogeneous catalytic tests where surface CO was observed over the same temperature range. Furthermore, $CH_4$ was detected in correspondence with the decomposition of formate and formation of the Cu phase, with a maximum conversion rate of 2.8 % measured at 470 °C (on completely reduced copper), supporting the indication of independent reaction pathways for the conversion of $CO_2$ to $CH_4$ and CO that was

suggested by catalytic tests. The resulting Cu NPs had a final crystallite size of ca. 44 nm at 500 °C and retained a significantly active surface.

Keywords: CuO, EXAFS, DRIFTS, XRD, $CO_2$ hydrogenation, DFT, Continuous Hydrothermal Flow

## 1. Introduction

Anthropogenic activities have led to a rise in greenhouse gases such as $CO_2$ in the atmosphere of over 40 % since the industrial revolution, with more than half of this increase occurring over the last 50 years,[1] which is considered to be the main cause of climate change.[2,3] In tandem with $CO_2$ sequestration and storage, conversion of $CO_2$ to useful products such as methanol, formic acid, methane and CO, is an appealing way to overcome the $CO_2$ problem and utilise $CO_2$ as an alternative carbon source to conventional fossil fuels. Formic acid has many applications in the leather and textile industry and recently it has been shown that it is possible to store hydrogen in formic acid via the reduction of $CO_2$.[4,5] Other value-added chemicals from $CO_2$ conversion include methanol and methane, which can be used as a feedstock for the chemical industries.[3] A feasible approach for $CO_2$ conversion is to use it in combination with hydrogen gas from renewable sources. Hydrogenation has been shown to effectively yield formic acid, methanol, methane and higher hydrocarbons mostly in heterogeneous processes at temperatures in the range 200 - 550 °C.[2]

Among many catalysts studied for $CO_2$ hydrogenation, copper-based materials are a well-known system for converting $CO_2$ with high efficiencies and selectivity.[2] Industrially, $Cu/ZnO/Al_2O_3$ is employed with a syngas mixture ($CO/CO_2/H_2$) at temperatures 250 – 300 °C and 50 – 100 bar pressure.[6,7] Under these conditions, methanol is the thermodynamically favoured product, while under atmospheric pressure conditions, it favours carbon monoxide via the reverse water gas shift reaction (RWGS).[8]

There is still a lack of understanding about the interplay between the active phase(s) of copper, surface species and gas products, as the catalyst is progressively reduced over a large interval of temperature. These relationships become increasingly complex when considering structural changes and the effects that more reducing or oxidising conditions have on the surface atom valence and reactivity. Many techniques have been employed to investigate speciation and corresponding oxidation states for both industrial and model copper catalysts, usually relying on complex oxidation/reduction pathways by $CO_2$ and $CO$ starting from $Cu(0)$ as the catalyst. Another complication is related to the presence and role of support oxides such as $ZnO$, $Al_2O_3$, $SiO_2$ or $ZrO_2$, whose possible synergistic contributions introduce a further element of uncertainty when trying to assess the net properties of the copper catalyst.

Several methods have been explored to synthesise copper-based catalysts, including precipitation methods,[9] impregnation, decomposition of copper substrates,[10] solid-state[11], microwave assisted wet routes,[12] and batch hydrothermal[13] syntheses. These methods are generally performed in batch and their scale up is technically challenging, costly and intrinsically prone to batch-to-batch variations. On the other hand, continuous powder processes are well-established, reliable and can be relatively inexpensive, but only for the production of coarser particulates.[14] Continuous Hydrothermal Flow Synthesis (CHFS) is a promising and scalable method ($kg\ h^{-1}$) for the manufacture of nanoparticles, typically in the size range of 1-50 nm.[15] The CHFS process involves mixing of superheated water (generally above its critical point $T_c = 374\ °C$ and $p_c = 22.1\ MPa$) with a flow of an aqueous metal salt solution (at ambient temperatures) in an engineered mixer, which can efficiently mix the two feeds and avoid blockages.[16,17] This method has produced an extensive range of high-purity nanomaterials, consistently and with tailored compositions.[18–21]

Herein, we report the synthesis of small copper(II) oxide nanoparticles (11 nm) prepared via CHFS at a production rate of kg day$^{-1}$. Such production scale allowed for the distribution of nanoparticles originating from the very same sample to be tested across multiple laboratories and techniques that performed the characterisation. In particular, the as-prepared CuO nanoparticles were studied as $CO_2$ hydrogenation catalysts by combining multiple analytical techniques: Diffuse Reflectance Infrared Fourier Transform Spectroscopy (DRIFTS), Extended X-ray Absorption Fine Structure (EXAFS), X-Ray Diffraction (XRD) and catalytic testing were employed under analogous experimental conditions to understand the structure-product relationships as the catalyst structure transformed from CuO to Cu via $Cu_2O$. The in-situ DRIFTS experiments were performed in a flow of $CO_2/H_2/Ar$ and the surface product speciation was studied as the temperature was raised from 20 to 500 °C. In-situ XRD and EXAFS studies were conducted under similar conditions to investigate the concurrent phase transformation from CuO to Cu, and determine a correlation between phase and observed products. Heterogeneous catalysis experiments were performed to assess and quantify the gaseous product yields, especially after the stabilization of the catalyst at temperatures > 250 °C. Finally, density functional theory (DFT) based calculations were carried out on the $CO_2$ hydrogenation processes on the CuO surfaces and compared with the experimental results to suggest the potential mechanisms of the formate formation and subsequent $CO/CH_4$ conversion on the observed catalyst phases.

## 2. Experimental

2.1. Materials: Copper(II) sulfate pentahydrate ($CuSO_4 \cdot 5H_2O$, technical grade, >98 %) and potassium hydroxide pellets (KOH) were supplied from Sigma Aldrich (Dorset, UK). Sodium pyrophosphate decahydrate ($Na_4P_2O_7 \cdot 10H_2O$, technical grade 99 %) was supplied by Alfa Aesar (Lancashire, UK). Deionised water (> 10 MΩ) was used for all the experiments.

2.2. Synthesis of copper(II) oxide nanoparticles

Pure copper(II) oxide nanoparticles were synthesised in a lab-scale CHFS system, the details of which are described elsewhere (Figure S1).[22] The process consists of four high pressure diaphragm pumps providing four separate pressurised feeds into two different sized Confined Jet Mixers (CJM)[23] in series. The first CJM is where the nanoparticles were formed and the secondary CJM was used to quench the CuO nanoparticles. A room temperature aqueous solution of 50 mM copper sulfate pentahydrate was pumped (via pump 2, 40 mL min$^{-1}$) to mix with an aqueous flow of 0.1 M potassium hydroxide solution (via pump 3, 40 mL min$^{-1}$) in a tee piece. The resulting solution was subsequently mixed with a superheated water feed at 400 °C (via pump 1, 80 mL min$^{-1}$) in CJM 1 (Figure S1). This CJM was designed to eliminate any possible blockages under common experimental conditions and to enable rapid turbulent mixing of the incoming hot and cold feeds (Reynolds number, Re ≈ 6000). The calculated mixing temperature was ca. 305 °C, resulting in a residence time of 0.61 s before the nanoparticle slurry was rapidly quenched as it mixed with a feed of room temperature aqueous solution of 1 w/v % $Na_4P_2O_7$ (via pump 4, 160 mL min$^{-1}$) in CJM 2 (Figure S1).

The as-formed nanoparticle slurry was cooled in-flow via a cold-water jacketed pipe and was continuously collected from the exit of a backpressure regulator valve, which maintained the pressure of the whole system at 24 MPa (Tescom model 26-1700, Tescom BPR, Hamilton, UK). The particle slurry was cleaned through multiple cycles of centrifugation and dialysis until the conductivity of the slurries was less than 50 M$\Omega^{-1}$. The concentrated aqueous slurry was then freeze-dried and slowly heated from -40 °C to 25 °C in a VirTis Genesis 35 XL Lyophilizer at ca. $10^{-7}$ MPa for 24 hours.

2.3. Characterisation of nanopowders

The freeze-dried nanopowder was examined by powder X-ray diffraction (Bruker D4 diffractometer, Cu K$_{\alpha 1}$, $\lambda = 1.54$ Å). Brunauer-Emmett-Teller (BET) surface area measurements were carried out using N$_2$ in a Micrometrics ASAP 2420 apparatus. The sample was degassed at 150 °C for 12 hours in nitrogen before measurements. Chemical analysis was carried out using a Thermo Scientific K-Alpha X-ray photoelectron spectrometer (XPS, Al Kα at 1.487 keV). Survey scans were conducted at a pass energy of 150 eV and high-resolution region scans were conducted at 50 eV. The XPS spectra were processed using Casa™ software. The binding energy scale was calibrated by the C 1s peak at 285.0 eV. Detailed morphology and size analysis was carried out using high-resolution transmission electron microscopy (TEM). Images were obtained on a JEOL JEM 2100 TEM with 200 keV accelerating voltage and a LaBF$_6$ filament. For HRTEM measurements, samples were prepared by dispersing the particles ultrasonically in methanol 99.9 % (Sigma Aldrich, Dorset UK) and dropping the resulting dispersion onto 300 mesh Holey copper film grids (Agar Scientific, UK). Particle size distributions were determined by measuring the diameter of 150 particles from TEM images.

2.4. Heterogeneous catalytic testing

Activity tests of the catalyst were carried out in a continuous flow reactor, described elsewhere.[24,25] NDIR/O$_2$ multichannel measurement was used for the analysis of CH$_4$, CO, CO$_2$, O$_2$, (NGA 2000 Rosemount Analytical MLT-½-Analyzer). H$_2$ was detected with a Thermal Conductivity Detector (TCD, Rosemount Analytical HYDROS 100) connected in series.

The volume concentrations of H$_2$ and CO$_2$ were kept constant throughout the experiment at 16% and 4% respectively, with N$_2$ as balance. The unsupported CuO powder (~ 400 mg) was loaded in a quartz tubular reactor ($\phi = 6$ mm) and the temperature cycled between room temperature and 500 °C; the heating and cooling ramps were specular and the rates fixed at 6 °C min$^{-1}$. The catalyst bed length

was approximately 15 mm. The weight hourly space velocity (WHSV) was varied between 4900 mL $h^{-1}$ $g^{-1}$ and 70000 mL $h^{-1}$ $g^{-1}$, calculated based on the weight of the unreduced CuO nanopowder. The total gas flow rate ranged between 30 mL $min^{-1}$ and 365 mL $min^{-1}$.

## 2.5. DRIFTS experiments

DRIFTS experiments were performed on a Bruker Vertex 70 FTIR spectrometer with a liquid $N_2$ cooled detector. The sample (~50 mg) was placed in a ceramic crucible in an *in situ* DRIFTS cell fitted with ZnSe windows and connected to stainless steel gas lines. The *in situ* DRIFTS spectra were recorded with a resolution of 4 $cm^{-1}$ and with an accumulation of 56 scans every 30 seconds during the temperature ramp. The IR data were analysed by the OPUS software and are reported as log $1/R$, where $R$ is the sample reflectance. During the DRIFTS studies, the temperature of the material was increased from 20 to 500 °C measured by a thermocouple placed in the catalyst bed. The spectrum of the sample at room temperature under flowing argon was taken as the background. Before the measurements, the samples were treated in a flow at 100 mL $min^{-1}$ of a 50:50 mixture of dry 5 % $H_2$ in Ar and $CO_2$ at 30 °C for 1 h. The temperature was ramped from 20 to 500 °C, at 5 °C $min^{-1}$.

## 2.6. XRD/EXAFS experiments

In-situ XRD and EXAFS measurements were performed on the Dutch-Belgian beamline (BM01b) at the ESRF in Grenoble. Monochromatic radiation was supplied by a double Si (111) crystal monochromator, ion chambers measured incident and transmitted beam intensities ($I_0$ and $I_t$), and fluorescence was measured using a 13-element germanium solid-state detector. All measurements were acquired at the copper K-edge (8980 eV). The nanopowder (~10 mg) was loaded in a capillary tube through which 5 % $H_2$ in He was flowed at 20 mL $min^{-1}$. The temperature was ramped from 20 °C to 500 °C at 5 °C $min^{-1}$. The EXAFS spectra were acquired for 3 minutes and the XRD patterns

for 20 s at regular temperature stages. XAS data reduction and Linear Combination Analysis with non-linear, least-squares minimization was performed with the software package Horae Athena.[26]

2.7 Computational methods

All calculations were performed using the Vienna Ab-initio Simulation Package (VASP) with a plane-wave basis set.[27–30] The projector augmented wave (PAW) method was used to describe the interaction between ions and electrons,[31] and the non-local exchange correlation energy was evaluated using the Perdew−Burke−Ernzerhof functional.[32,33] The Hubbard model was used to treat strong correlations within the DFT + $U$ method in the Dudarev formalism.[34]

Recently, we have determined a value of U that can efficiently describe both copper I and II oxides[35] and this effective U value of 7 eV was selected for the localized 3d electrons of Cu. The atomic structures were relaxed using the tetrahedron method with Bloch correction as implemented in VASP[28] and the positions of all the atoms in the cell were fully relaxed until the atomic forces on each ion were less than 0.01 eV Å$^{-1}$. To model $CO_2$ hydrogenation, we have used our earlier bulk and surface models of CuO,[35] where at the base of the surface simulation cell, two layers of atoms were fixed at their relaxed bulk positions to simulate the bulk phase of the crystal, while above these two layers, the surface was represented by two layers of atoms whose positions were allowed to change freely during optimization.

We have further used the implementation of the DFT-D2 approach described by Grimme[36] to account for long-range dispersion forces. We sampled the (1x1) surface cells with a 5x5x1 Monkhorst-Pack[37] k-point mesh, while (2x2) supercells were modelled with 2x2x1 k-point mesh.

The adsorption energy per molecule was calculated from the relation

$$E_{ads} = E_{surf+mol} - (E_{surf} + E_{mol})$$

where $E_{surf+mol}$ is the total energy of the adsorbate-substrate system, $E_{surf}$ is the energy of the naked surface slab, and $E_{mol}$ is the energy of the isolated molecule. Within this definition, a negative adsorption energy indicates an exothermic process. In order to calculate $E_{mol}$, we modelled the isolated molecule in the centre of a broken symmetry cell with lattice constants of 20 Å, sampling only the Gamma-point of the Brillouin zone with the same accuracy parameters as described for the surfaces. In the case of co-adsorption and reaction on the surface, the relative energies were computed with respect to the sum of the total energies of the corresponding free molecules. We have used the improved dimer[38,39] and climbing image nudge elastic band (CI-NEB) methods[40] to calculate the activation energy barriers.

## 3.Results and Discussion

### 3.1. Synthesis of CuO

CuO was synthesised via CHFS, where a flow of supercritical water (400 °C, 24 MPa) mixed with a feed of ambient aqueous metal salt solution in a CJM. When a flow of supercritical water and a flow of metal salt mix in a turbulent regime, the resulting supersaturation of metal ions determines a rapid nucleation of nanoparticles through hydrolysis and dehydration of the metal ions with a concurrent metal oxide formation, in a two-step process extensively described by Adschiri et al.[41–45]

The as prepared copper(II) oxide nanoparticles were characterised by powder XRD (Figure 1). All peaks were representative of the monoclinic C/2c symmetry of cupric oxide (tenorite, JCPDS 01-089-2529). The analysis of the three most intense peaks [111, -111 and 202] yielded an average crystallite size of $11 \pm 2$ nm. The measured BET surface area was $75 \pm 5$ m$^2$ g$^{-1}$, in good agreement with an expected surface area of 79 m$^2$ g$^{-1}$ calculated by the hard-sphere approximation.
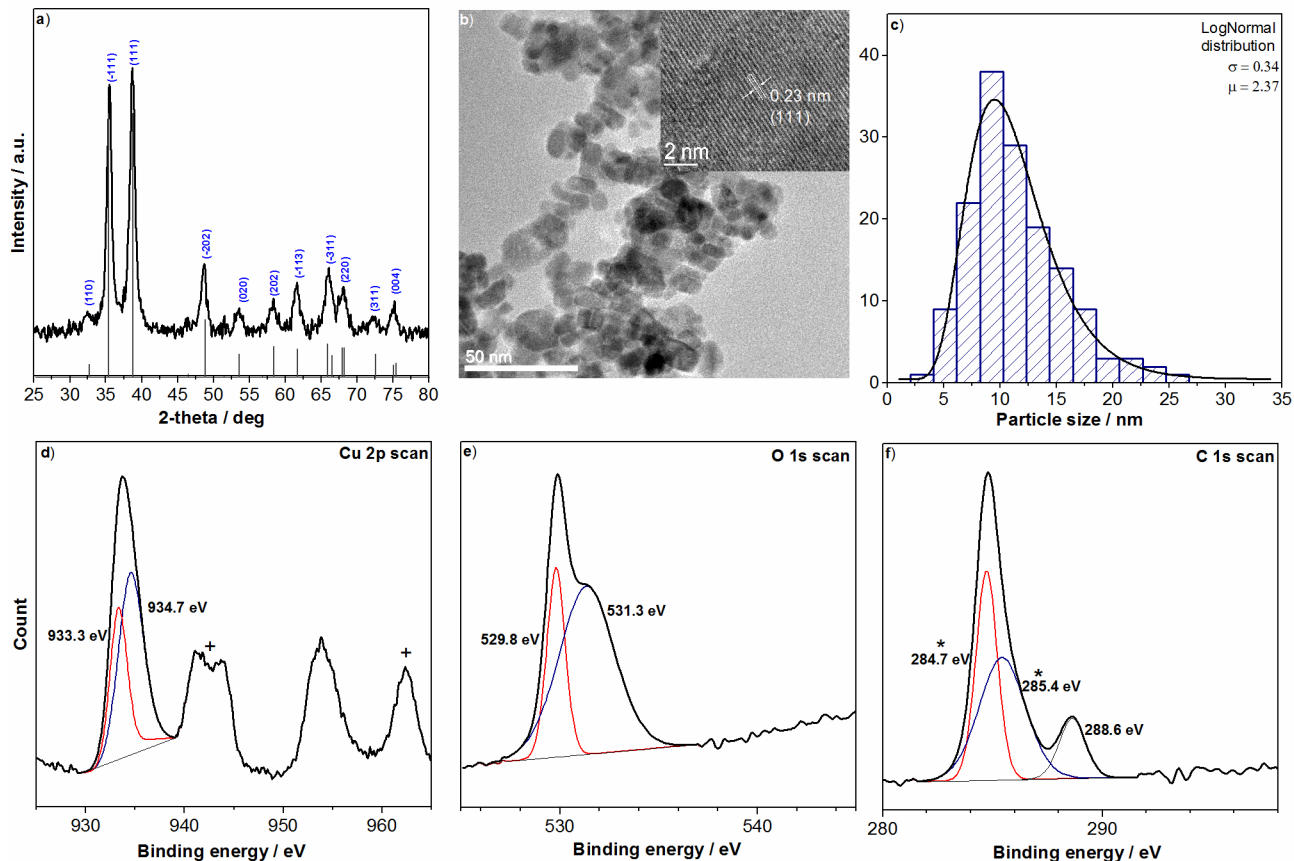
Figure 1 – Structural and surface characterisation of the as-synthesised CuO nanopowders. a) XRD pattern (monoclinic CuO, tenorite, JCPDS 01-089-2529). b) Bright field TEM image with HRTEM insert. c) Histogram of the particle size distribution as measured from TEM with lognormal fit (average size = 11 ± 4 nm). d) XPS scan for Cu 2p1/2 (953.5 eV) and Cu 2p3/2 (933.6 eV). Strong satellite peaks denoted as +. e) XPS scan for O 1s with peaks at 529.8 eV (Cu-O) and 531.3 eV (carbonate). f) XPS scan for C 1s with peaks at 284.7 eV, 285.4 eV (adventitious carbon) and 288.6 eV (carbonate).

The surface oxidation state of the copper in the as-synthesised nanoparticles was analysed by XPS to confirm the compositional nature of the nanoparticles and verify the presence of possible surface contaminants deriving from the preparation process. High-resolution scans of the Cu 2p core level

spectrum (Figure 1c) represented the Cu $2p_{3/2}$ peak (at 933.6 eV) and Cu $2p_{1/2}$ (at 953.5 eV). The "shake up" satellite confirmed the existence of the Cu (II) oxidation state (marked as +), which is seen with open $3d^9$ shell systems and is distinctive of certain transition metal compounds that have unpaired electrons in the 3d shell. This is not present with other Cu oxidation states ($Cu^+$ and $Cu^0$) and matches well with reported XPS data on CuO.[46,47] The core level O and C 1s spectra were further analysed, (Figure 1e and f). The O 1s scan showed the deconvoluted peaks indicating the peak at 529.8 eV associated with the oxygen in a Cu-O bond and another peak at 531.3 eV associated with the O in carbonate species. Further confirmation of the presence of carbonate species was also observed in the C 1s spectrum, where the deconvolution of the peaks showed three contributions, two of which were associated with adventitious carbon usually present in XPS samples (marked as *). The C associated with the carbonate was observed at 288.6 eV. The carbonate species present on the surface of the CuO were associated with the adsorption of atmospheric $CO_2$ after exposure of the sample to air.

The morphology, size and crystallinity of the CuO nanoparticles were examined by TEM (Figure 1b and c). The particles had a rounded morphology and appeared to be slightly aggregated. HRTEM images (Figure 1b, insert) showed that the NPs were monocrystalline. Observed lattice planes with a spacing of 0.23 nm corresponded to the (111) plane and were consistent with literature values of 0.23 nm[48] and the powder XRD pattern (Figure 1a), indicating that CuO prepared by CHFS was highly crystalline despite a process residence time between the initial mixing and quenching phase of less than a second. The particle sizes observed from TEM followed a log-normal distribution with an average size of $11 \pm 4$ nm (Figure 1c, measured from 150 particles, log-normal parameters: $\mu = 2.37$, $\sigma = 0.34$), in agreement with the XRD Scherrer analyses. The as obtained CuO nanoparticles were investigated as catalysts for $CO_2$ hydrogenation.

3.2. Catalytic testing

In order to assess the product speciation and yields, heterogeneous catalysis testing was performed on CuO nano-powders from the original batch. In the experimental tests, the reagent ratio in the gas stream was fixed at the stoichiometric one (nominal: 16% $H_2$, 4% $CO_2$, 80% $N_2$; 5 °C min$^{-1}$) with $H_2$:$CO_2$ = 4, assuming the reaction proceeds as

$$CO_2 + 4H_2 \rightarrow CH_4 + 2H_2O \qquad \Delta G_{298} = -114 \text{ kJ mol}^{-1} \ (1)$$

The WHSV was varied across a large range (4900 - 70000 mL h$^{-1}$ g$^{-1}$) to qualitatively determine relative conversion behaviours and products.
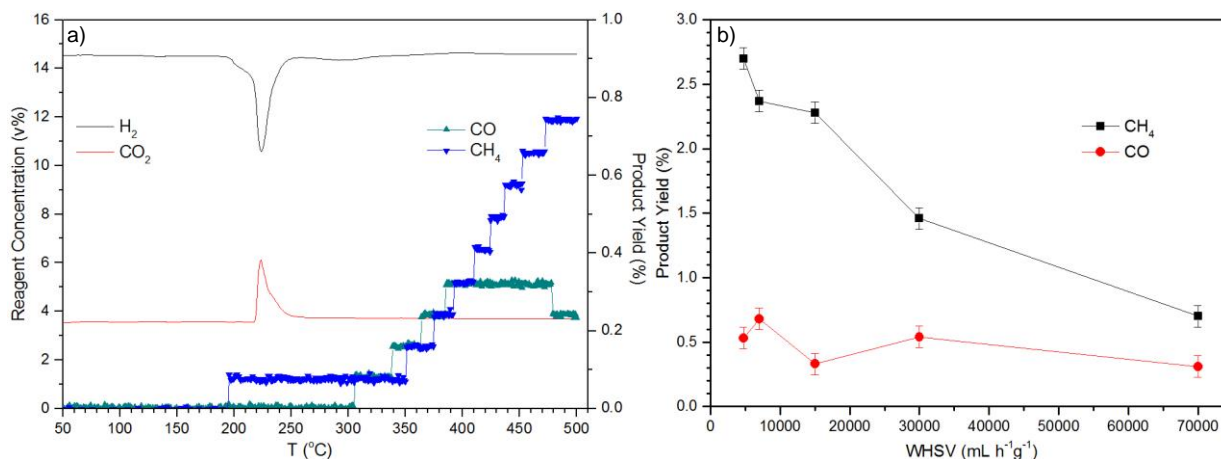


Figure 2 – $CO_2$ hydrogenation, heterogeneous catalysis tests for CuO-based nanocatalysts. a) Reagent concentration and product conversion yield vs temperature (50 -500 °C, WHSV = 70000 mL h$^{-1}$ g$^{-1}$). b) Product conversion yield vs WHSV for $CH_4$ and CO.

The compositional profile of the gas phase with increasing temperature showed minimal variations for any considered gas species up to 170 °C. At this temperature, hydrogen depletion was observed in the gas stream, which was attributed to the onset of the bulk reduction of CuO to $Cu_2O$ (up to 190 °C) and additionally of $Cu_2O$ to Cu (from 170 to 270 °C). The molar amount of consumed $H_2$ is

quantitatively in good agreement with the expected stoichiometry for the CuO to Cu reduction. Interestingly, the reduction was accompanied by an increase in $CO_2$, which was possibly associated with the release of adsorbed $CO_2$ with concurrent surface conversion. This behaviour was observed for any WHSV, and is shown in Figure 2a for a WHSV of 70000 mL h$^{-1}$ g$^{-1}$, which closely approximated the WHSVs of the subsequent DRIFTS, EXAFS and XRD experiments. In fact, the experimental configurations adopted for these characterisations imposed a few limitations on the accessible WHSVs, which were estimated to be relatively high at 120000 mL h$^{-1}$ g$^{-1}$.

Hydrogen conversion also determined the initial point at which methane was detected, possibly via the hydrogenation of formate.[49] Methane conversion increased appreciably once the catalyst reduction was complete at T > 300 °C, and reached a maximum value at the highest tested temperature of 500 °C. Carbon monoxide was detected starting at T = 310 °C.

While the reaction consistently yielded mixtures of CO and $CH_4$ under any tested conditions, the relative ratio of $CH_4$:CO strongly depended on the WHSV (Figure 2b). In particular, the ratio increased for decreasing WHSV, showing that low velocities favoured the formation of $CH_4$, with a maximum $CO_2$ conversion to $CH_4$ at 4900 mL h$^{-1}$ g$^{-1}$ equal to 2.7%; the conversion of $CO_2$ to CO on the other hand varied over a much narrower range, with little dependence on the WHSV and values equalled to 0.5 ± 0.2 %. This behaviour determined the maximisation of the $CH_4$:CO ratio at low WHSVs, with a maximum $CH_4$:CO = 5.1 at 4900 mL h$^{-1}$ g$^{-1}$ (Figure S4). The trends of the products shown in Figure 2b, suggested that the $CH_4$ and CO yields were independent from each other, possibly because the methanation and gas shift reactions run in parallel over the catalyst.


3.3. DRIFTS analysis: $CO_2$ hydrogenation

14

The catalytic behaviour of the as-synthesised CuO nanoparticles in the presence of $CO_2$ and $H_2$ in Ar was studied by Diffuse Reflectance Infrared Fourier Transform Spectroscopy (DRIFTS). The nanopowdered catalyst was loaded in the DRIFTS measurement cell and flushed with a $CO_2/H_2$ in Ar gas mixture (50 % $CO_2$, 2.5% $H_2$, 47.5 % Ar) for one hour at room temperature to remove air and stabilise the sample with respect to the reactive gas mixture. The temperature was subsequently ramped up at 5 $^{\circ}C$ $min^{-1}$ up to 500 °C and spectra were continuously acquired to assess changes on the sample surface. At 70 °C, the evolution of three peaks at 2850, 2920 and 2970 $cm^{-1}$ indicated the presence of formate species, attributed to the C-H stretching mode and the C-H bending mode combinations,[50–52] which suggested that a reaction between $CO_2$ and $H_2$ on the surface of the nanoparticles had taken place at relatively low temperatures. The maximum intensity of these peaks was observed at 190 °C and no formate peak was detected at temperatures above 210 ºC (Figure 3 and 4a).
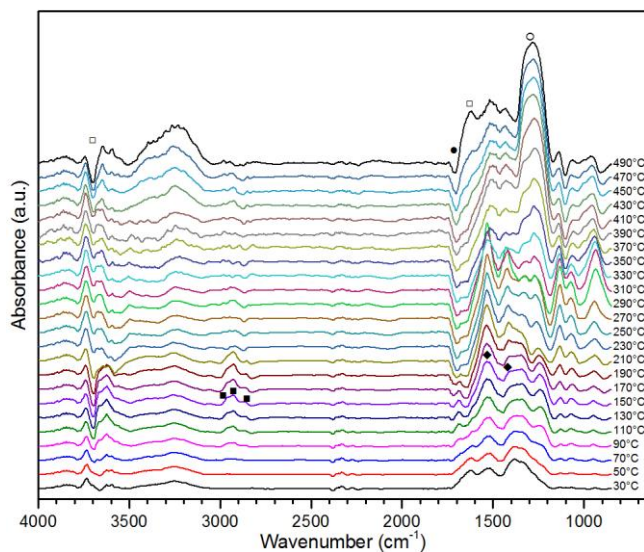


Figure 3 – DRIFTS spectra of the as-prepared CuO nanocatalyst as the temperature is raised from 50 ºC to 500 ºC with a heating rate of 5 °C $min^{-1}$, under a flow of 2.5 % $H_2$, 47.5 % Ar and 50 % $CO_2$. Symbols: □ water/hydroxyl, ■ formate, ● hydrogencarbonate, ◆ monodentate carbonate, ○ bidentate carbonate.

Concurrently with the formate production, a negative peak in the region around 3700 cm$^{-1}$ appeared, which was assigned to the removal of surface hydroxyls. Starting at 150 °C, the spectra showed a further, set of negative peaks that were assigned to the loss of adsorbed molecular water (1640 cm$^{-1}$) and surface bicarbonates (1685 and 1430 cm$^{-1}$) that were initially formed as a consequence of exposure of the sample to the atmosphere.[53–55] In contrast, monodentate carbonate absorption bands related to the O-C-O vibrational modes appeared at 1400 and 1530 cm$^{-1}$ between 110 - 350 °C, but could not be detected at higher temperatures.[52] Indeed, for T > 350 °C, peaks associated to bidentate surface carbonates became more evident, with a large band between 1200 cm$^{-1}$ and 1350 cm$^{-1}$ which remained the only detectable IR absorption peak for carbon species up to the final temperature of 490 °C.

Carbon monoxide was detected at 2150 cm$^{-1}$ between 250 and 310 °C with a relatively weak signal (Figure 4b), in perfect agreement with the catalytic tests where CO desorption was observed for the same temperatures (Figure 2a), and reached a maximum in the gas phase at 380 °C. This wavelength is usually attributed to $Cu^+$-CO species, as when CO is bound to $Cu^0$ sites the observed wavenumber is usually lower;[56] the broad nature of the observed peak anyway didn't allow to provide an unambiguous assignment. The formation of CO was attributed to the reverse water gas-shift (RWGS) reaction as shown in equation (2),

$$CO_2 + H_2 \rightarrow CO + H_2O \qquad\qquad (2)$$

which was also confirmed by the corresponding transient replenishment of the adsorbed water peak centered at 3700 cm$^{-1}$ (Figure 3).
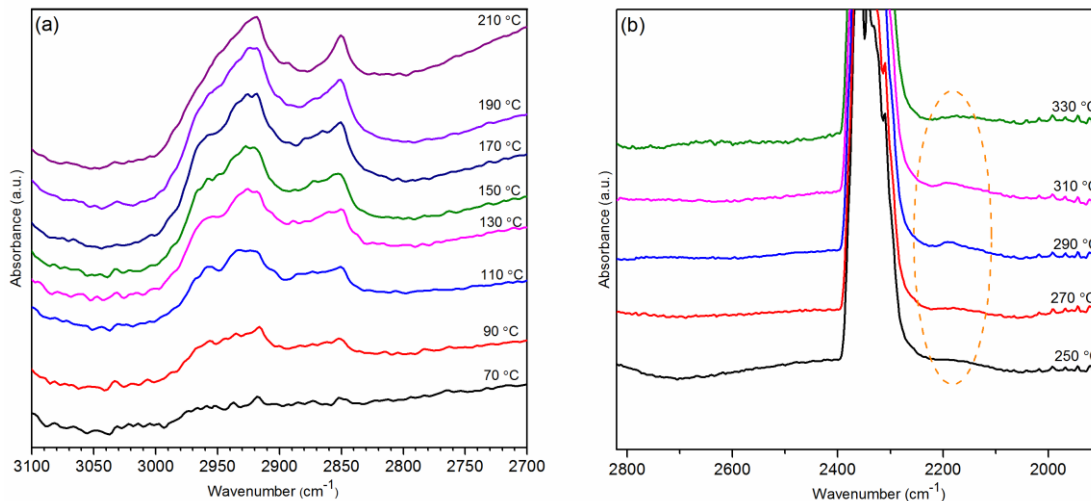
Figure 4 – Selected ranges for wavenumber and temperature for the DRIFTS spectra with (a) evolution with temperature of the formate peaks and (b) evolution with temperature of the CO peak.

Once the DRIFTS experiments were completed, the sample extracted from the analysis cell was observed to be red, confirming that under the experimental conditions used, the initial copper(II) oxide had reduced to copper(0). The nature and progression of the reduction process was studied via a combination of EXAFS and XRD studies.

### 3.4. XRD and EXAFS Studies

To further understand the relationship between structure and product speciation, the CuO particles were analysed by in-situ synchrotron XRD and EXAFS techniques at the European Synchrotron Radiation Facility (ESRF) in Grenoble. The experimental conditions were set to mimic the DRIFTS experiments, so as to be able to unequivocally assign specific reactivity and surface speciation to a particular crystalline structure. A previous set of experiments performed ex-situ in flowing $H_2$, with and without $CO_2$, showed that the reducing nature of $H_2$ and the lack of $H_2O$ in the gas stream, prevented the formation of bulk copper carbonate species such as malachite, azurite or pure $CuCO_3$.

All the acquired XRD patterns were refined to identify crystalline phases and determine average crystallite sizes via application of the Rietveld method.
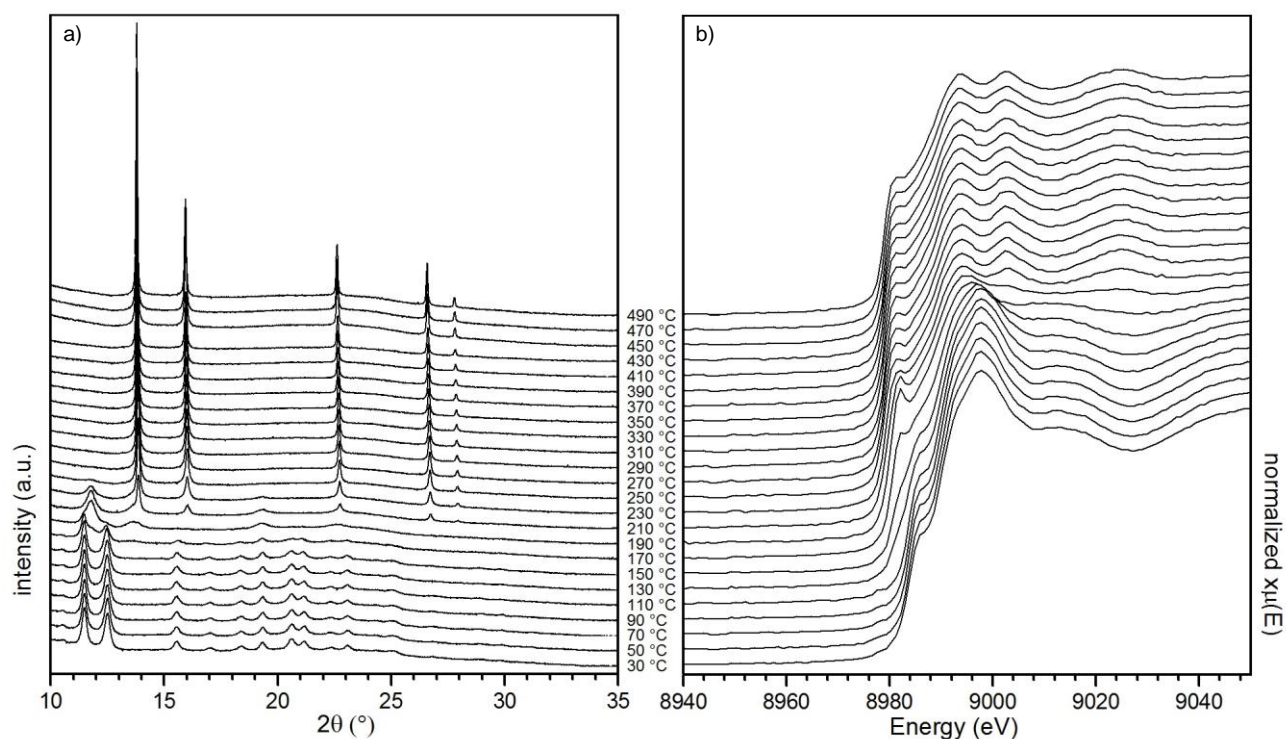


Figure 5 - Synchrotron-based measurements: a) powder XRD patterns and b) EXAFS spectra for CuO nanopowders, as the temperature was raised from 50 to 500 $^{\circ}$C at a heating rate of 5 $^{\circ}$C min$^{-1}$, under a flow of 5 % $H_2$ in He.

At room temperature, the diffraction pattern identified the sample as being CuO (reference pattern: JCPDS 01-080-0076) and matched the Cu k$\alpha$ XRD data for as-synthesised CuO nanoparticles (Figure 5a and 1a). As the temperature was increased, the pattern remained largely unchanged up to 170 $^{\circ}$C; thereafter the first phase transformation was observed as $Cu_2O$ peaks appeared (JCPDS 00-005-0067). The CuO average particle size was concurrently stable at 11 ± 2.0 nm (Figure 6a) up to the onset of the reduction process that led to the formation of $Cu_2O$ crystalline domains; these particles grew in size with temperature at the expenses of CuO phases as inferred by the narrowing of

the diffraction peaks. CuO domains were completely extinct at 190 ºC, when $Cu_2O$ was the only detectable phase with an average crystallite size of 6 nm. At this stage, evidently each CuO nanoparticle was replaced by multiple smaller $Cu_2O$ crystallites, as could be deduced by comparison of crystallite sizes and by the progression of the relative proportions of the two distinct phases (Figure 6a).

As the temperature was further increased, peaks due to metallic copper were initially observed at 190 ºC, when a mixture of $Cu_2O$ and Cu crystallites co-existed, which grew in size up to 230 °C. Beyond this point, $Cu_2O$ domains were rapidly reduced to Cu, which was the only detected species at temperatures > 250 ºC (JCPDS 00-004-0836). Cu nanocrystallites steadily grew up to an average size of 44 ± 4 nm at 500 ºC (Figures 5a and 6a).
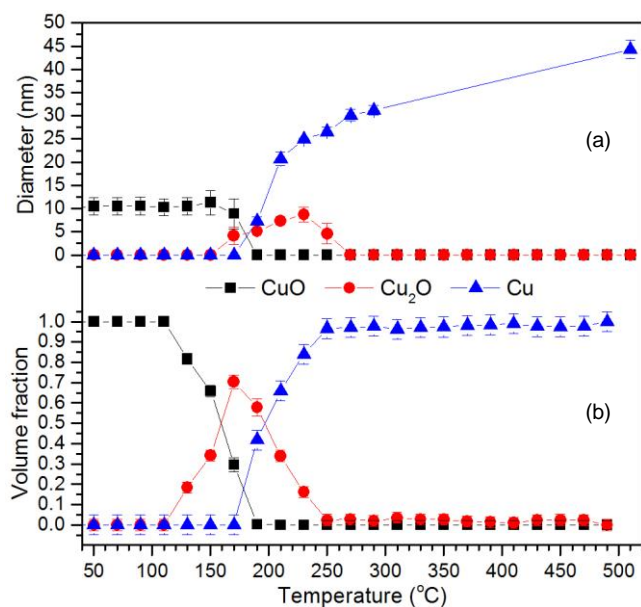


Figure 6 –Crystallite sizes determined from Rietveld analysis of synchrotron XRD patterns (a) and phase composition as determined by Linear Combination Analysis (non-linear, least squares minimization method) from EXAFS data (b) for the tested CuO-based nanocatalyst as the temperature is raised from 50 ºC to 500 ºC.

The isolation and presence of each phase was further confirmed by EXAFS analysis (Figure 5b and 6b); at 130 $^\circ$C, changes in local structure of CuO occurred by 170 $^\circ$C, a distinctive 1s-4s peak emerged at the edge associated with $Cu_2O$. At 190 $^\circ$C, the 1s 4s peaks were sharpest, indicative of pure phase $Cu_2O$. As the $Cu_2O$ was reduced to Cu, the spectrum was identical to that expected for the pure metal by 250 $^\circ$C (JCPDS 00-004-0836).

Both EXAFS and XRD results were in complete agreement with the catalytic tests results, as the phase transitions (CuO to $Cu_2O$ and then to Cu) and gas reactant ($H_2$) consumption were observed for the very same temperature ranges, thus confirming that the experimental conditions adopted for the different techniques were consistent and the relative results were comparable.

## 3.5  DFT Calculations

The CuO (111) surface, as identified in the experiment, is the most stable surface and found to be dominant in the crystal morphology (Figure 1).[35] The top layer consists of 3- and 4-coordinated Cu and O atoms. 3-coordinated O atoms ($O_{SUF}$) are the most exposed atoms, each connected to one 3-coordinated (coordinatively unsaturated -$Cu_{CUS}$) and two 4-coordinated (coordinatively saturated -$Cu_{CSA}$) Cu atoms as shown in Figure S2. The interaction of the $H_2$ molecule with the CuO(111) surface in a (2x2) supercell was first investigated by placing the molecule close to different surface atoms in all possible orientations. In all the input configurations attempted, the $H_2$ molecule moved away from the surface, except in the case when it was placed near the surface oxygen $O_{SUF}$, whereupon it adsorbed with a calculated binding energy of -57.9 kJ $mol^{-1}$. The $Cu_{CUS}$ atom moved up from the surface, thereby elongating its bond to an $O_{SUB}$ atom from 1.922 to 2.068 Å. The $O_{SUF}$ atom broke its bond to the surface copper atom, $Cu_{CSA}$, and connected with the $H_2$ to form a surface-bound water molecule as shown in Figure 7a, as was also found by Maimaiti et al.[57]  The O-H bond lengths in this water molecule were 0.974 and 1.005 Å, while ∠HOH was 107.6°. A comparison with recent

work on $CO_2$ activation on the CuO(111) surface,[35] revealed that the binding of the $H_2$ molecule was weaker compared to the adsorption of the $CO_2$ molecule, which bonded to a surface oxygen, $O_{SUF}$, with an adsorption energy of -71.4 kJ mol$^{-1}$.[35]
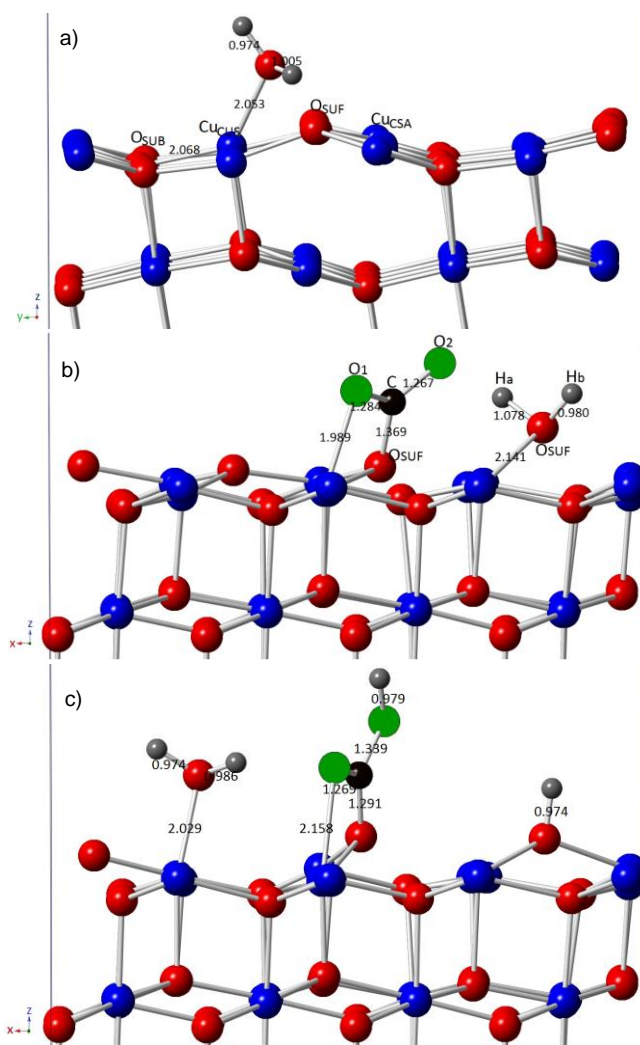


Figure 7 – a) The $H_2$ molecule interaction with the CuO(111) surface. b) $CO_2$ and $H_2$ molecule co-adsorption on the CuO(111) surface. c) The formation of carboxyl, together with water and hydroxyl species on the CuO(111) surface. Bond length values are in Å. Blue and red colour balls indicate Cu and O surface atoms respectively, while O, C and H atoms of the molecule are represented by green, black and grey coloured balls, respectively.

The co-adsorption of the $CO_2$ and $H_2$ molecules on the CuO (111) surface in a (2x2) supercell was then investigated. As a starting point, the geometry of the pre-adsorbed $CO_2$ molecule on the surface was used and the $H_2$ molecule was placed close to the $CO_2$ molecule at different surface sites. Here, the $H_2$ molecule also interacted in a similar fashion and was bound to surface oxygen, $O_{SUF}$, forming a water molecule as shown in Figure 7b. One of the H atoms ($H_a$) of the formed water molecule oriented towards the $CO_2$ molecule, resulting in a stretching of the O-H bond to 1.078 Å. These attractive interactions were observed between the hydrogen atom of the water molecule and an oxygen atom of the $CO_2$ molecule, resulting in increased activation of the $CO_2$ and $H_2O$ molecules. It should be noted that the $CO_2$ and $H_2O$ molecules underwent further structural transformation as ∠OCO and ∠HOH changed to 127.5° and 105.9°, respectively, from their values of 133.2° and 107.6°, respectively in the isolated adsorbed molecules. Consistent with the attractive interactions, an increased binding energy of this $CO_2$–$H_2$ co-adsorption configuration was noted at -179.3 kJ mol$^{-1}$, which was larger than the fairly weak binding of the separately adsorbed $CO_2$ and $H_2$ molecules. As a next step towards modelling the $CO_2$ hydrogenation, different configurations were explored to attach a hydrogen atom to the $CO_2$ molecule, thereby breaking one of the O-H bonds of the water molecule leaving a surface-bound O-H species bonded to $O_{SUF}$, was investigated, However, after relaxation, the H atom reconnected with the O-H to re-form the water molecule. Further hydrogenation of the surface resulted in a similar formation of another water molecule and an increase in the overall binding energy of the co-adsorbed species to -252.3 kJ mol$^{-1}$, indicating attractive interactions between the molecules (Figure S3). After the formation of the second water molecule, it was found that breaking the O-H bond of one of the water molecules, resulted in the formation of a carboxyl species, as shown in Figure 7c. The formation of a formate species was found to be unfavourable, as all initial configurations with a hydrogen atom attached to the carbon atom optimized to form the

carboxyl species. Moreover, a low activation barrier of 61.8 kJ mol$^{-1}$ was required for the formation of the carboxyl species. Our calculations thus suggested that formate was unlikely to be formed on pristine CuO (111) crystallographic facets, which was in marked contrast to $CO_2$ hydrogenation behaviour on the $Cu_2O$ (111) surface, where it was recently found that the carboxyl species are unlikely to form with a high activation barrier of > 400 kJ mol$^{-1}$. In contrast, on the $Cu_2O$ (111) surface, formate was a favourable intermediate, which could be obtained via a low activation barrier of ~12 kJ mol$^{-1}$.[58] The consistent experimental observation of formate species at low temperatures can therefore be considered a strong indication of the rapid reduction of the surface CuO layer to a phase richer in Cu(I) centres. On such surfaces, the adsorption energy for formate was calculated to be -198.9 kJ mol$^{-1}$, which is much larger than what was calculated for water (-116.9 kJ mol$^{-1}$) and $CO_2$ (-57.0 kJ mol$^{-1}$) and which may make the release from the surface difficult, favouring its decomposition or conversion to other products.

### 3.6. Structure-product relationship

Experimental data analysis was performed by combining the information collected across all the considered analytical techniques, and subsequently compared to DFT predictions. Nano-powders belonging to the same batch from the flow reactor were employed throughout these tests in order to eliminate possible sample differences. Identical or near-identical experimental conditions (gas composition and flow rate, temperature interval and ramp) were applied in the different experimental techniques, in accordance with the relative limitations and experimental apparatus.

As a first observation, the DRIFTS analysis suggested $CO_2$ reduction to formate initially took place on CuO surfaces (Figure 8), as CuO was the only phase detected at 70 °C by both XRD and EXAFS. As the temperature was raised, the CuO to $Cu_2O$ phase transition occurred, via equation (3)

$$2CuO + 2H^+ + 2\ e^- \rightarrow Cu_2O + H_2O, \hspace{3cm} (3)$$

The above reaction (3) coincided with the formation of monodentate carbonate species at the surface starting at 110 ºC. Despite the competing presence of carbonates on the surface,[54] the formate peak intensity kept growing up to 190 ºC, remarkably following the behaviour of the $Cu_2O$ phase volume fraction as determined by the EXAFS-LCA analysis. Unlike other reports that were performed in isothermal conditions under similar reducing atmospheres,[59] our experimental conditions allowed to clearly isolate and identify the intermediate $Cu_2O$ phase, thus providing some insight on its specific activity in relation to the $CO_2$ conversion to formate.

The observation of formate species on the catalyst surface by DRIFTS at low temperatures, and therefore in a range where no $Cu_2O$ was detected by either XRD or DRIFTS, can be explained by considering the intrinsic characteristics of both XRD and EXAFS. As the reduction proceeded from the surface of the nano-particle, it is safe to assume that reduced $Cu_2O$ domains were present at temperatures < 170 °C, where the earliest $Cu_2O$ XRD peaks were measurable and quantifiable in crystallites of ~4 nm (Figure 5a). Indeed, this assumption was supported both experimentally and computationally; EXAFS data showed that local extended $Cu_2O$-coordination was already present at 130 °C (Figure 4b and 5b), indicating the formation of reduced clusters too small to be positively detected by XRD; DFT modelling showed that surface reduction could have taken place as soon as the surface was exposed to $H_2$ (Figure 7a), with the immediate formation of a $H_2O$ molecule through the cleaving of a Cu-O bond. The surface encountered by the oncoming $CO_2$ molecule was therefore oxygen-depleted, and progressively transforming from CuO to $Cu_2O$, with the concurrent increase in the formate signal. The relatively low temperatures prevented significant particle sintering at this stage, and allowed the catalyst to retain a large specific surface area and consequently a large volume density of active sites, resulting in a clear DRIFTS signal for formates.

As the temperature was further increased, both EXAFS and XRD started to confirm the onset of the reduction of $Cu_2O$ to $Cu$ at 190 °C, via equation (4)

$$Cu_2O + 2H^+ + 2e^- \rightarrow 2Cu + H_2O \tag{4}$$
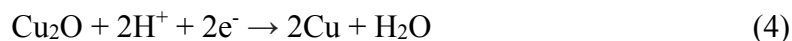
At 190 °C, the formate peak intensity reached its maximum (Figure 8), CuO was no longer detected while $Cu_2O$ and $Cu$ were present at a volume ratio of 3:2. XRD/EXAFS suggested that $Cu_2O$ was completely converted to $Cu$ by 250 °C, with a rapid decrease in volume fraction that is closely matched by a corresponding decrease in formate signal intensity (Figure 8).

Under the experimental conditions used, formate can essentially undergo two reaction pathways on the newly formed copper surface: decomposition to $CO_2$ and $H_2$[60] or hydrogenation to $CH_4$. Heterogeneous tests showed that the earliest trace of $CH_4$ was measured at 190 °C (Figure 6a), matching the initial observation of Cu(0) both from EXAFS and XRD and the concurrent depletion of $H_2$ in the gas stream (Figure 5a). The detection of $CH_4$ with $H_2$ and formate depletion might therefore indicate that at this stage formate was converted to methane via

$$HCOO^- + 3.5H_2 \rightarrow CH_4 + 2H_2O \tag{5}$$

According to both reactions (1) and (5), methane formation was expected to provide water as a secondary product, which was detected by DRIFTS as hydroxyls (3700 $cm^{-1}$, O-H stretching) and adsorbed molecular species (1630 $cm^{-1}$, $\delta H_2O$). A reaction pathway that includes a formate intermediate for the methanation of $CO_2$ has been consistently reported for Ni-based (Sabatier's reaction) and other catalysts:[61–66] this work suggests that analogous pathways may be feasible on Cu-based catalysts in milder conditions. An alternative decomposition pathway for formate could not be

entirely excluded, as a rapid increase in the $CO_2$ concentration was also measured in the gas stream starting at 220 °C (Figure 6a). Even if the largest fraction of this peak could be ascribed to hydrogencarbonate and carbonate species decomposition, a contribution from the decomposition of formate was still possible.

$CH_4$ underwent an appreciable increase in conversion yield from 350 °C, closely following an increase of CO production in the gas stream. In agreement with previous reports,[49] the desorption of CO might have made metal sites available for direct $CO_2$ hydrogenation to methane, with no formate intermediates. DRIFTS spectra confirmed the presence of CO on the catalyst surface up to 310 °C, when CO is desorbed and beyond which carbonates remain as the only detectable species up to the highest tested temperature of 500 °C. In particular, monodentate carbonate species were completely eliminated by 350 ºC, being progressively replaced by bidentate species.

While the detailed mechanisms for $CO_2$ methanation with hydrogen are still highly debated,[67,68] a few possible pathways have been proposed, including the presence of formate, CO, $CH_xO$ and C intermediates.[49,61–63,69] It was observed that for the described experimental conditions, the detection of methane was complementary to the detection of formate on the catalyst surface, and they were in turn strongly correlated to a specific copper phase, with formate closely following the $Cu_2O$ phase evolution and $CH_4$ following the formation of Cu.

The unsupported catalyst as metallic copper, was stable for temperatures > 250 °C, with the sole structural variation consisting in the Cu crystallite size growth via sintering for increasing temperatures, as observed by EXAFS and XRD (Figure 5). No copper carbonate, hydroxycarbonate or hydride species were detected. In relation to the gaseous products observed over this temperature range, the $CH_4$ and CO maximum conversion yields appeared to be unrelated at different WHSVs; CO showed minimal variations across an extended WHSV range and $CH_4$ formation was favoured at

lower velocities. The CH4:CO ratio improved accordingly from ~2 to > 5 as WHSV went from 70000 to 4900 mL h$^{-1}$ g$^{-1}$.
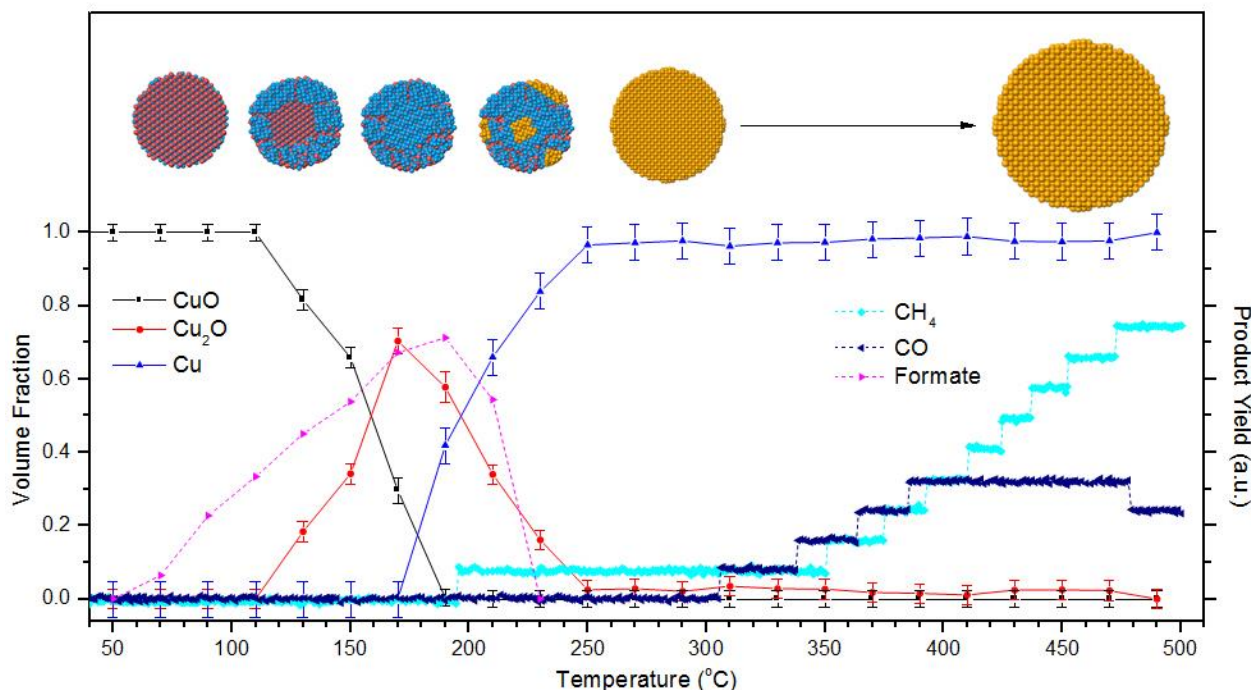


Figure 8 – Comparison between phase composition (from EXAFS-LCA data analysis) and product yield (in arbitrary units for comparison purposes; formate as measured from DRIFTS, CH4 and CO as measured from heterogeneous catalytic testing) vs temperature for CuO-based catalysts. The top scheme summarises the structural evolution of the catalyst with temperature, with blue, red and yellow spheres representing Cu(I)/Cu(II), O and Cu(O) atoms, respectively.

## 4. Conclusions

In this work, continuous hydrothermal flow method enabled the large scale production of catalyst nanopowders, so that the same synthetic batch could be employed for all the experimental characterisations. No catalyst support was used to exclude any potential external contribution to the observed reactions. The product speciation for copper-based catalysts in the CO$_2$ hydrogenation

reaction was studied over a wide range of temperatures, by combining EXAFS, XRD, DRIFTS and heterogeneous catalysis tests, with the support of DFT computational simulations. A consistent set of experimental conditions was adopted, in terms of thermal treatments, gas compositions and space velocities.

The results were remarkably coherent across all of the employed techniques, and under the reported experimental conditions the production of formate, methane and carbon monoxide was proven to be strongly correlated to the formation and the conversion of specific crystalline phases. In particular, formate was observed in association with the reduction of $CuO$ to $Cu_2O$, while the further reduction of $Cu_2O$ to $Cu$ determined the concurrent onset of $CH_4$ and $CO$ production. DFT calculations of potential $CO_2$ hydrogenation processes on $CuO$, in combination with previous results for $Cu_2O$ surfaces,[58] concurred fully with the experimental findings that the formation of formate took place on $Cu_2O$. The calculations suggested that $CO_2$ hydrogenation to formate was unlikely to occur on a pristine $CuO$ surface, where the carboxyl intermediate was more favourable. However, as the $H_2$ molecule rapidly reduced the $CuO$ (111) surface by forming a water molecule, it generated a reduced $Cu_2O$ surface where the formation of formate was highly favoured. The complementary observation of formate depletion and initial $CH_4$ detection indicated that under the chosen experimental conditions, the hydrogenation of formate to methane was indeed feasible starting at 190 °C, although the direct hydrogenation of $CO_2$ with the concurring decomposition of formate couldn't be excluded. The initial product yield for methane was relatively low and constant up to 350 °C, when it started to increase with temperature on pure $Cu(0)$ surfaces. Similarly, $CO$ was detected both in DRIFTS and heterogeneous catalysis experiments, with a conversion yield that steadily increased between 300 °C and 400 °C, whereupon it reached a plateau. The maximum conversion yield for $CH_4$ was found to be strongly dependent on the WHSV as it increased for decreasing WHSVs, unlike

CO whose behaviour was relatively unaffected by varying WHSVs, suggesting the presence of two parallel reaction pathways on the copper surface and maximum selectivity for the lowest WHSV. Finally, the unsupported catalyst in the copper phase presented a post-treatment crystallite size of 44 nm, thus retaining a significant active surface.

Supporting Information. Schematic representation of the Continuous Hydrothermal Flow Synthesis (CHFS) process, DFT model surfaces, and heterogeneous test results for WHSV = 4900 mL h$^{-1}$ g$^{-1}$.

AUTHOR INFORMATION

**Corresponding Author**

*E-mail: j.a.darr@ucl.ac.uk. Telephone: +44 (0)20 7679 4345

**Author Contributions**

‡These authors contributed equally.

References

(1)     Cicerone, R. J.; Nurse, P. *Climate Change Evidence and Causes*; National Academy of Sciences, **2014**.

(2)     Wang, W.; Wang, S.; Ma, X.; Gong, J. *Chem. Soc. Rev.* **2011**, *40*, 3703–3727.

(3)     Ganesh, I. *Mater. Sci. Forum* **2013**, *764*, 1–82.

(4)     Lu, X.; Leung, D. Y. C.; Wang, H.; Leung, M. K. H.; Xuan, J. *ChemElectroChem* **2014**, *1*, 836–849.

(5)     Enthaler, S.; von Langermann, J.; Schmidt, T. *Energy Environ. Sci.* **2010**, *3*, 1207.

(6)     Beyond Oil and Gas: The Methanol Economy, Second Edition - Olah - Wiley Online Library http://onlinelibrary.wiley.com/book/10.1002/9783527627806 (accessed Feb 23, 2016).

(7)     *Handbook of Heterogeneous Catalysis*; Ertl, G., Knözinger, H., Schüth, F., Weitkamp, J., Eds.; Wiley-VCH Verlag GmbH & Co. KGaA: Weinheim, Germany, **2008**.

(8)     Skrzypek, J.; Lachowska, M.; Serafin, D. *Chem. Eng. Sci.* **1990**, *45*, 89–96.

(9)     Zhu, J.; Bi, H.; Wang, Y.; Wang, X.; Yang, X.; Lu, L. *Mater. Chem. Phys.* **2008**, *109*, 34–38.

(10)    Lin, Z.; Han, D.; Li, S. *J. Therm. Anal. Calorim.* **2012**, *107*, 471–475.

(11)    Vidyasagar, C. C.; Venkatesha, T. G.; Viswanatha, R. *Nano-Micro Lett.* **2012**, 73–77.

(12)    Yang, C.; Xiao, F.; Wang, J.; Su, X. *Sensors Actuators, B Chem.* **2015**, *207*, 177–185.

(13)    Neupane, M. P.; Kim, Y. K.; Park, S.; Kim, K. a.; Lee, M. H.; Bae, T. S. *Surf. Interface Anal.* **2009**, *41*, 259–263.

(14)    *Nanomaterials: synthesis, properties, and applications*; Edelstein, A. S., Cammarata, R. C.,

Eds.; CRC Press, **1998**.

(15)   Byrappa, K.; Adschiri, T. *Prog. Cryst. Growth Charact. Mater.* **2007**, *53*, 117–166.

(16)   Tighe, C. J.; Gruar, R. I.; Ma, C. Y.; Mahmud, T.; Wang, X. Z.; Darr, J. a. *J. Supercrit. Fluids* **2012**, *62*, 165–172.

(17)   Tighe, C. J.; Cabrera, R. Q.; Gruar, R. I.; Darr, J. A. *Ind. Eng. Chem. Res.* **2013**, *52*, 5522–5528.

(18)   Cabanas, A.; Darr, J. A.; Poliakoff, M.; Lester, E. *Chem. Commun.* **2000**, No. 11, 901–902.

(19)   Goodall, J. B. M.; Illsley, D.; Lines, R.; Makwana, N. M.; Darr, J. A. *ACS Comb. Sci.* **2014**.

(20)   Goodall, J. B. M.; Kellici, S.; Illsley, D.; Lines, R.; Knowles, J. C.; Darr, J. a. *RSC Adv.* **2014**, *4*, 31799–31809.

(21)   Weng, X.; Perston, B.; Wang, X. Z.; Abrahams, I.; Lin, T.; Yang, S.; Evans, J. R. G.; Morgan, D. J.; Carley, A. F.; Bowker, M.; Knowles, J. C.; Rehman, I.; Darr, J. A. *Appl. Catal. B Environ.* **2009**, *90*, 405–415.

(22)   Gruar, R. I.; Tighe, C. J.; Darr, J. A. *Ind. Eng. Chem. Res.* **2013**, *52*, 5270–5281.

(23)   Darr, J. A.; Tighe, C. J.; Gruar, R. I. Co-current mixer, apparatus, reactor and method for precipitating nanoparticles. US9192901, May 30, 2015.

(24)   Lanza, R.; Järås, S. G.; Canu, P. *Appl. Catal. A Gen.* **2007**, *325*, 57–67.

(25)   Lanza, R.; Bersani, M.; Conte, L.; Martucci, A.; Canu, P.; Guglielmi, M.; Mattei, G.; Bello, V.; Centazzo, M.; Rosei, R. *J. Phys. Chem. C* **2014**, *118*, 25392–25402.

(26)   Ravel, B.; Newville, M.; IUCr; B., R.; J., R. J.; D., C. S.; G., B.; T., C. C.; T., C. D.; D., L.; W., E.; B., R.; J., S.; M., H.; A., S. M.; A., F.; J., G.; S., H.; F., A.; I., B.; L., H. B.; M., G. E.; C., D. J.; S., K.; K., K.; D., F.; M., B.; B., B.; N., Y.; A., K.; P., F.; A., F.; A., A.; J., T.; T., U.; A., M.; G., V.; M., N.; M., N.; P., L.; Y., Y.; J., R. J.; A., S. E.; M., N.; B., R.; D., H.; J., R. J.; A., S. E.; Y., Y.; B., R.; J., R. J.; C., A. R.; I., Z. S.; J., R. J.; A., A.; C., A. R.; J., E. M. *J. Synchrotron Radiat.* **2005**, *12*, 537–541.

(27)   Kresse, G.; Hafner, J. *Phys. Rev. B* **1993**, *47*, 558–561.

(28)   Kresse, G.; Hafner, J. *Phys. Rev. B* **1994**, *49*, 14251–14269.

(29)   Kresse, G.; Furthmüller, J. *Comput. Mater. Sci.* **1996**, *6*, 15–50.

(30)   Kresse, G.; Furthmüller, J. *Phys. Rev. B Condens. Matter Mater. Phys.* **1996**, *54*, 11169.

(31)   Blochl, P. E. *Phys. Rev. B* **1994**, *50*, 17953–17979.

(32)   Perdew, J. P.; Burke, K.; Ernzerhof, M. *Phys. Rev. Lett.* **1996**, *77*, 3865–3868.

(33)   Perdew, J. P.; Burke, K.; Ernzerhof, M. *Phys. Rev. Lett.* **1997**, *78*, 1396.

(34)   Dudarev, S. L.; Savrasov, S. Y.; Humphreys, C. J.; Sutton, A. P. *Phys. Rev. B* **1998**, *57*, 1505–1509.

(35)   Mishra, A. K.; Roldan, A.; de Leeuw, N. H. *J. Phys. Chem. C* **2016**, *120*, 2198–2214.

(36)   Grimme, S. *J. Comput. Chem.* **2006**, *27*, 1787–1799.

(37)   Monkhorst, H. J.; Pack, J. D. *Phys. Rev. B* **1976**, *13*, 5188–5192.

(38)   Henkelman, G.; Jónsson, H. *J. Chem. Phys.* **1999**, *111*, 7010.

(39)  Heyden, A.; Bell, A. T.; Keil, F. J. *J. Chem. Phys.* **2005**, *123*, 224101.

(40)  Henkelman, G.; Uberuaga, B. P.; Jónsson, H. *J. Chem. Phys.* **2000**, *113*, 9901.

(41)  Adschiri, T.; Hakuta, Y.; Arai, K. *Ind. Eng. Chem. Res.* **2000**, *39*, 4901–4907.

(42)  Hakuta, Y.; Onai, S.; Terayama, H. *J. Mater. Sci. Res.* **1998**, *17*, 1211–1213.

(43)  Hakuta, Y.; Adschiri, T.; Suzuki, T. *J. Am. Ceram. Soc.* **1998**, *64*, 2461–2464.

(44)  Adschiri, T.; Kanazawa, K.; Arai, K. *J. Am. Ceram. Soc.* **1992**, *75*, 2615–2618.

(45)  Adschiri, T.; Kanazawa, K.; Arai, K. *J. Am. Ceram. Soc.* **1992**, *75*, 2615–2618.

(46)  Chen, H.; Zhao, G.; Liu, Y. *Mater. Lett.* **2013**, *93*, 60–63.

(47)  Ethiraj, A. S.; Kang, D. J. *Nanoscale Res. Lett.* **2012**, *7*, 70.

(48)  Nikam, A. V; Arulkashmir, A.; Krishnamoorthy, K.; Kulkarni, A. A.; Prasad, B. L. V. *Cryst. Growth Des.* **2014**, *14*, 4329–4334.

(49)  Marwood, M.; Doepper, R.; Renken, A. *Appl. Catal. A Gen.* **1997**, *151*, 223–246.

(50)  Burch, R.; Chalker, S.; Pritchard, J. *J. Chem. Soc. Faraday Trans.* **1991**, *87*, 193.

(51)  Millar, G. J.; Rochester, C. H.; Howe, C.; Waugh, K. C. *Mol. Phys.* **1992**, *76*, 833–849.

(52)  Le Peltier, F.; Chaumette, P.; Saussey, J.; Bettahar, M. M.; Lavalley, J. C. *J. Mol. Catal. A Chem.* **1998**, *132*, 91–100.

(53)  Chinchen, G. C.; Denny, P. J.; Jennings, J. R.; Spencer, M. S.; Waugh, K. C. *Appl. Catal.* **1988**, *36*, 1–65.

(54)  Bailey, S.; Froment, G. F.; Snoeck, J. W.; Waugh, K. C. *Catal. Letters* **1995**, *30*, 99–111.

(55)  Busca, G.; Lorenzelli, V. *Mater. Chem.* **1982**, *7*, 89–126.

(56)  Millar, G. J.; Rochester, C. H.; Waugh, K. C. *J. Chem. Soc. Faraday Trans.* **1991**, *87*, 1467.

(57)  Maimaiti, Y.; Nolan, M.; Elliott, S. D. *Phys. Chem. Chem. Phys.* **2014**, *16*, 3036–3046.

(58)  Mishra, A. K.; de Leeuw, N. H. *J. CO2 Util.* **2016**.

(59)  Rodriguez, J. A.; Kim, J. Y.; Hanson, J. C.; Pérez, M.; Frenkel, A. I. *Catal. Letters* **2003**, *85*, 247–254.

(60)  Nakano, H.; Nakamura, I.; Fujitani, T.; Nakamura, J. *J. Phys. Chem. B* **2001**, *105*, 1355–1365.

(61)  Schild, C.; Wokaun, A.; Koeppel, R. A.; Baiker, A. *J. Phys. Chem.* **1991**, *95*, 6341–6346.

(62)  Schild, C.; Wokaun, A.; Baiker, A. *Fresenius. J. Anal. Chem.* **1991**, *341*, 395–401.

(63)  Weigel, J.; Koeppel, R. A.; Baiker, A.; Wokaun, A. *Langmuir* **1996**, *12*, 5319–5329.

(64)  Pan, Q.; Peng, J.; Wang, S.; Wang, S. *Catal. Sci. Technol.* **2014**, *4*, 502–509.

(65)  Schild, C.; Wokaun, A.; Baiker, A. *J. Mol. Catal.* **1990**, *63*, 223–242.

(66)  Schild, C.; Wokaun, A.; Baiker, A. *J. Mol. Catal.* **1991**, *69*, 347–357.

(67)  Wei, W.; Jinlong, G. *Front. Chem. Sci. Eng.* **2010**, *5*, 2–10.

(68)  Tu, W.; Zhou, Y.; Zou, Z. *Adv. Mater.* **2014**, *26*, 4607–4626.

(69)  Lapidus, A. L.; Gaidai, N. A.; Nekrasov, N. V.; Tishkova, L. A.; Agafonov, Y. A.; Myshenkova, T. N. *Pet. Chem.* **2007**, *47*, 75–82.

**Table of Contents Graphic**